

2017

Internal Wave Scattering in Continental Slope Canyons, Part 2: A Comparison of Ray Tracing and Numerical Simulations

Robert Nazarian
Fairfield University, rnazarian@fairfield.edu

Sonya Legg

Follow this and additional works at: <https://digitalcommons.fairfield.edu/physics-facultypubs>

Copyright © 2017 The Author(s). Published by Elsevier Ltd.

This work is licensed under an Attribution-NonCommercial-NoDerivatives 4.0 International (CC BY-NC-ND 4.0)

The final publisher PDF has been archived here with permission from the copyright holder.

Peer Reviewed

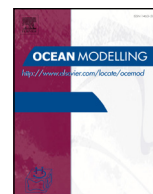
Repository Citation

Nazarian, Robert and Legg, Sonya, "Internal Wave Scattering in Continental Slope Canyons, Part 2: A Comparison of Ray Tracing and Numerical Simulations" (2017). *Physics Faculty Publications*. 138. <https://digitalcommons.fairfield.edu/physics-facultypubs/138>

Published Citation

Nazarian, R. H., & Legg, S. (2017). Internal wave scattering in continental slope canyons, Part 2: A comparison of ray tracing and numerical simulations. *Ocean Modelling*, 118, 16-30. <https://doi.org/10.1016/j.ocemod.2017.07.005>

This item has been accepted for inclusion in DigitalCommons@Fairfield by an authorized administrator of DigitalCommons@Fairfield. It is brought to you by DigitalCommons@Fairfield with permission from the rights-holder(s) and is protected by copyright and/or related rights. **You are free to use this item in any way that is permitted by the copyright and related rights legislation that applies to your use. For other uses, you need to obtain permission from the rights-holder(s) directly, unless additional rights are indicated by a Creative Commons license in the record and/or on the work itself.** For more information, please contact digitalcommons@fairfield.edu.



Internal wave scattering in continental slope canyons, Part 2: A comparison of ray tracing and numerical simulations



Robert H. Nazarian*, Sonya Legg

Program in Atmospheric and Oceanic Sciences, Princeton University, Princeton, NJ 08540, USA

ARTICLE INFO

Article history:

Available online 4 August 2017

Keywords:

Internal waves
Canyons
Mixing
Ray tracing

ABSTRACT

When internal waves interact with topography, such as continental slopes, they can transfer wave energy to local dissipation and diapycnal mixing. Submarine canyons comprise approximately ten percent of global continental slopes, and can enhance the local dissipation of internal wave energy, yet parameterizations of canyon mixing processes are currently missing from large-scale ocean models. As a first step in the development of such parameterizations, we conduct a parameter space study of M2 tidal-frequency, low-mode internal waves interacting with idealized V-shaped canyon topographies. Specifically, we examine the effect of varying the canyon mouth width, shape and slope of the thalweg (line of lowest elevation) (i.e. flat bottom or near-critical slope). In Part 1 of this study (Nazarian and Legg, 2017a), we developed a ray tracing algorithm and used it to estimate how canyons can increase the wave Froude number, by increasing energy density and increasing vertical wavenumber. Here in Part 2 we examine the internal wave scattering in continental slope canyons using numerical simulations, and compare the results with the linear ray tracing predictions. We find that at intermediate canyon widths, a large fraction of incoming wave energy can be dissipated, which can be explained as a consequence of the increase in ray density and, for near-critical slope canyons, increase in vertical wave number, which leads to lower Richardson number followed by instability. Relative to a steep continental slope without a canyon, we find that V-shaped flat bottom canyons always dissipate more energy and are an effective geometry for wave trapping and subsequent energy loss. When both flat bottom canyons and near-critical slope canyons are made narrower, less wave energy enters the canyon, but a larger fraction of that energy is lost to dissipation due to subsequent reflections and wave trapping. There is agreement between the diagnostics calculated from the numerical model and the linear ray tracing, lending support for the use of linear theory to understand the fundamental dynamics of internal wave scattering in canyons.

© 2017 The Author(s). Published by Elsevier Ltd.

This is an open access article under the CC BY-NC-ND license.
(<http://creativecommons.org/licenses/by-nc-nd/4.0/>)

1. Introduction

Internal waves are efficient transmitters of energy across ocean basins. As internal waves propagate away from their generation site, they may encounter the continental slope, where they can break and lead to diapycnal mixing. One of the continental slope features that can induce wave breaking are continental slope canyons. Despite observations highlighting their potential to be a sink of internal tidal energy, continental slope canyons have been largely overlooked by the modeling community (Bosley et al., 2004; Bruno et al., 2006; Codiga et al., 1999; Gardner, 1989; Gordon and Marshall, 1976; Gregg et al., 2011; Hall and Carter, 2011;

Hotchkiss and Wunsch, 1982; Lee et al., 2009a; 2009b; Petrucio et al., 1998; Vlasenko et al., 2016; Waterhouse et al., 2013; Xu and Noble, 2009). Here, we put forth a parameter space sweep to better understand the processes involved in internal wave scattering and mixing in continental slope canyons.

In conducting this parameter space study of internal wave scattering in continental slope canyons, our overarching goal is to contribute to the development of parameterizations of mixing by internal wave breaking. Such parameterizations, regardless of the topography for which they are applied, are increasingly formulated in terms of the global energy budget for internal waves. Parameterizations have been developed from the entire lifecycle of internal waves; from their generation at regions of rough topography (Buijsman et al., 2012) to their propagation over ocean basins and interaction with other waves and eddies (MacKinnon et al., 2013; Polzin, 2008), as well as their eventual breaking at topographic

* Corresponding author.

E-mail address: rn2@princeton.edu (R.H. Nazarian).

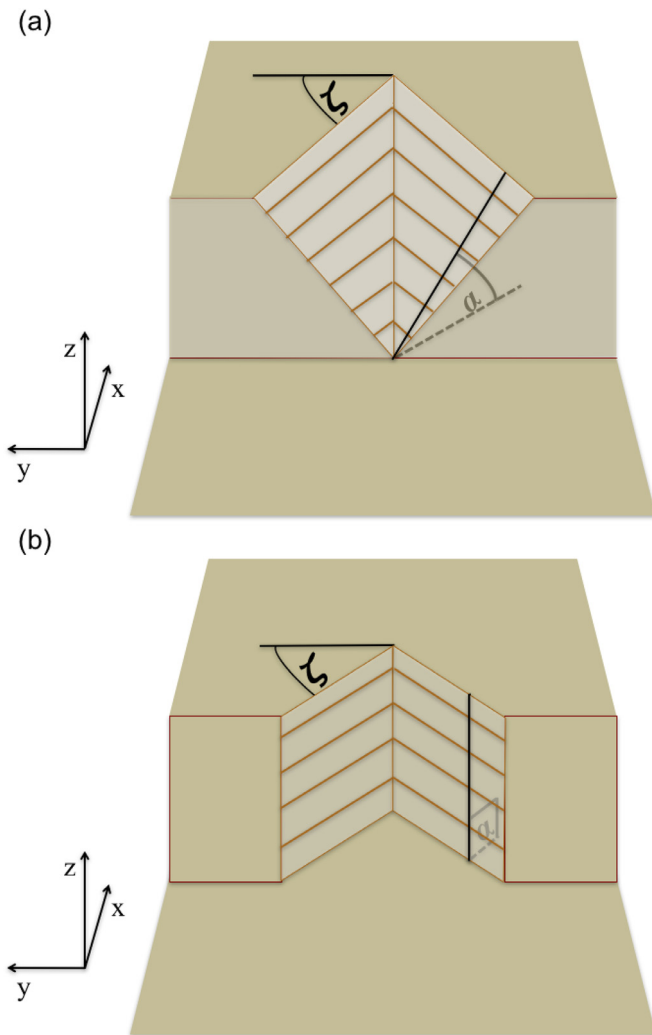


Fig. 1. Two classes of V-shaped canyons analyzed in this study. (a): near-critical slope canyon, (b): flat bottom canyon. Note that throughout our suite of experiments, angle ζ is varied identically for both class of canyons. Thus, the two different classes of V-shaped canyons are different in angle α only. The sidewalls of each canyon have isobaths, or lines of constant depth, drawn for clarity. (For interpretation of the references to color in this figure legend, the reader is referred to the web version of this article.)

features in the ocean interior or continental slope (Klymak et al., 2013; Legg, 2014). These studies have used a full internal wave energy budget to study the scattering effects of various, isolated, topographies (Klymak et al., 2013; Legg, 2014). By accounting for all terms in the energy budget, such studies have provided useful scalings for instability and turbulent dissipation based on properties of the topography; namely, the ratio of topographic height to the domain depth, the topographic width, and the relative topographic steepness. Given that mixing in the ocean is strongest around regions of varying topography (Polzin et al., 1997), and the location and magnitude of such mixing has ramifications for the large-scale ocean circulation (Melet et al., 2016), it is important for the formulation of ocean model mixing parameterizations to understand which and how topographic parameters modulate mixing. It is thus crucial to understand how much of the internal wave energy that encounters the continental slope topography is lost to mixing and dissipation. Our study analyzing the topographic dependence of internal wave dissipation is one component of this overall understanding.

Table 1
Summary of parameters of interest for all simulations.

α	ζ ($^\circ$)	H (m)	L (m)	ω^2 (10^{-8} s^{-2})	N^2 (10^{-6} s^{-2})
$\alpha_{\text{near-critical}}$	19.9	100	744	1.99	1.00
	26.1	100	744	1.99	1.00
	30.8	100	744	1.99	1.00
	35.9	100	744	1.99	1.00
	46.2	100	744	1.99	1.00
	52.3	100	744	1.99	1.00
	64.4	100	744	1.99	1.00
	73.5	100	744	1.99	1.00
	76.5	100	744	1.99	1.00
	80.0	100	744	1.99	1.00
	83.2	100	744	1.99	1.00
88.3	100	744	1.99	1.00	
90°	19.9	100	744	1.99	1.00
	26.1	100	744	1.99	1.00
	30.8	100	744	1.99	1.00
	35.9	100	744	1.99	1.00
	46.2	100	744	1.99	1.00
	52.3	100	744	1.99	1.00
	64.4	100	744	1.99	1.00
	73.5	100	744	1.99	1.00
	76.5	100	744	1.99	1.00
	80.0	100	744	1.99	1.00
	83.2	100	744	1.99	1.00
88.3	100	744	1.99	1.00	

While our study is motivated by observations of mixing in actual continental slope canyons, we begin by focusing on idealized V-shaped canyons in order to tease out the fundamental dynamics. In Part 1 of this study, we developed a ray-tracing algorithm which we used to explore the impact of canyon geometry on ray focusing and wave number in a linear context (Nazarian and Legg, 2017a). We used the ray tracing algorithm to gain a first-order understanding of the physical processes that can lead to instability in canyons as well as understand the regime where waves become nonlinear. Here in Part 2 we will compare the predictions of this linear ray tracing algorithm with fully nonlinear numerical simulations of internal waves scattering in identical canyon geometries using the Massachusetts Institute of Technology global circulation model (henceforth MITgcm). The idealized canyons we have chosen to analyze are oversimplifications of real canyon bathymetry; however our focus here is not to capture every detail of particular wave-topography interaction, but to explore the parameter space. In this part of our study, we explicitly diagnose the fraction of the incoming energy lost in the canyon, which is a quantity needed for parameterization development. The rationale for the V-shaped, idealized canyons that we have developed is described in Part 1.

The goal of this study is to understand the parameter dependence of internal wave energy dissipation and develop a physical framework to extend this theory to more realistic canyon topographies. We are particularly interested in the topographic parameters of canyon sidewall steepness (α) and canyon aspect ratio (ζ). In the process we seek to understand and predict the spatial structure of dissipation and determine the scenarios in which enhanced mixing is most likely. In this second part, we undertake a numerical parameter space study of idealized continental slope canyons and compare with theoretical predictions. We begin with a brief summary of the parameters of interest (covered in more detail in Nazarian and Legg, 2017a) in Section 2. In Section 3, we describe the MITgcm setup and how the model compares with the ray tracing algorithm developed in Part 1. We also provide a full summary of the calculations used to diagnose energy loss in the model. In Section 4, we take a holistic view of the parameter space, and use a combination of both the ray tracing and numerical simulations to construct an argument for the parameter dependence of internal wave breaking and dissipation in this idealized topography. We find that canyons are indeed efficient dissipators of incoming

internal wave energy. The primary mechanisms for energy loss in canyons are increases in ray density and vertical wavenumber. We additionally confirm the robustness of the ray tracing algorithm through comparison with the MITgcm.

2. Review of parameter space

In this study, we consider two parameters related to the topography. Specifically, we consider the canyon aspect ratio, or the canyon length relative to the canyon width, expressed through angle ζ . The second parameter that we consider is α , the canyon sidewall steepness. We are primarily interested in α as it compares to the internal wave slope (i.e. the relative topographic steepness). Omitting rotation, we express this steepness as

$$s = \frac{|\tan \alpha|}{|\omega/\sqrt{N^2 - \omega^2}|} \quad (1)$$

where N is the buoyancy frequency and ω is the wave frequency. For our simulations we consider the dominant tide, which is the lunar semidiurnal tide (M2).

We have two classes of V-shaped canyons, that are distinguished only by their thalweg steepness, α_t . The first class of canyons has a thalweg steepness that is near-critical and so, by construction, near-critical to supercritical sidewalls. The second class of canyons has vertical walls, which are thus very supercritical. The second parameter of interest is the canyon aspect ratio, ζ , which is varied systematically for both canyons (i.e. we run simulations for both classes of canyons for each ζ value). We modulate ζ by adjusting the canyon width only. Both canyons have a fixed height, H , of 100 m and a fixed length, L , of 744 m. See Fig. 1 for the geometry of the two canyon classes. In Fig. 1, isobaths, or lines of constant depth, are overlaid on the sidewalls to make clear that the canyons vary in α_t . Parameters of interest, both topographic and those for the wave and ambient fluid, are listed in Table 1, as well as their corresponding values for the submarine canyons considered in this study.

3. Methods

A two-pronged approach is taken to study the internal wave breaking dynamics in idealized V-shaped canyons: (i) a suite of numerical simulations using the MITgcm and (ii) a linear ray tracing algorithm using the theory developed in Part 1 (Nazarian and Legg, 2017a). When used in tandem, we can gain an understanding of the parameter space dependence of internal wave-driven mixing in these idealized canyons. Both the ray tracing algorithm and numerical simulations are set up identically for all canyon simulations, regardless of the topography class in which they fall. In Part 1 of this study (Nazarian and Legg, 2017a), we describe the ray tracing algorithm. Here, we provide an overview of the MITgcm numerical simulations.

A suite of numerical simulations is conducted using the MITgcm model (Marshall et al., 1997). The MITgcm is ideal for this problem due to its non-hydrostatic capabilities, arbitrary topography and open boundaries (Klymak et al., 2013; Legg, 2014; Legg and Adcroft, 2003; Nikurashin and Legg, 2011). All simulations are conducted in 3D (x, y, z) with flow allowed in all three directions. The lowest-mode internal wave is forced at the Western Boundary and propagates Eastward toward the variable canyon topography ($x = 0$), at which point it can reflect, scatter and refract. Any part of the wave that makes it past the topography is allowed to exit the domain at the Eastern Boundary via radiative (Orlanski) boundary conditions. The Southern and Northern boundaries ($y = -L_y/2$ and $y = +L_y/2$, respectively) are equipped with periodic boundary conditions. The Western boundary has a sponge layer 20 grid cells wide so that any wave that is reflected back from the topography

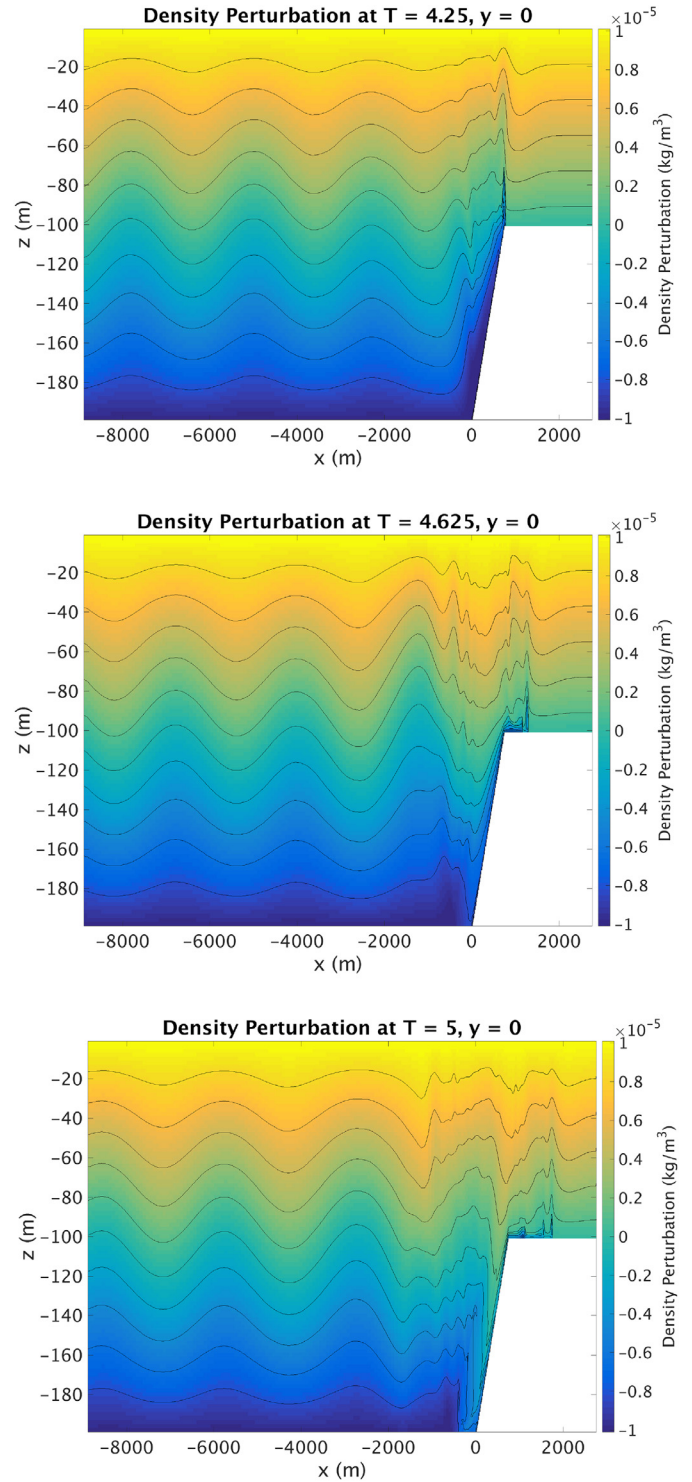


Fig. 2. Instantaneous snapshots of the density perturbation taken along the center of a near-critical slope canyon with $\zeta = 30^\circ$, taken at three equally spaced intervals over one tidal cycle (T): at (top) 4.25, (middle) 4.625 and (bottom) 5 tidal cycles, respectively. The wave propagates into the domain from the Western boundary, interacts with the topography and is allowed to radiate freely out through the Eastern boundary (x and y are aligned with longitude and latitude, respectively). Snapshots taken from the high-resolution simulation. (For interpretation of the references to color in this figure legend, the reader is referred to the web version of this article.)

towards the generation site does not impact the generation of the wave. We employ a no normal flow boundary condition, as well as a free slip boundary condition above the full bottom topography (i.e. flat ocean interior, continental slope canyon and shelf) and a linear free surface ($z = 0$).

The wave is forced with the M2 tidal frequency ($\omega = 1.41 \times 10^{-4} \text{ s}^{-1}$). We neglect the effects of rotation (i.e. $f = 0$); we discuss the assumption of no rotation in detail in Section 5). All simulations have a constant background density stratification of $N^2 = 10^{-6} \text{ s}^{-2}$. Since both ω and N^2 are fixed, the wave steepness is also fixed. Additionally, since the stratification is constant and the height of the canyon is half the height of the total ocean depth, by WKB scaling, these canyons are of similar effective vertical dimension to canyons in the real ocean in which there is non-uniform stratification, with largest stratification concentrated near the surface. This yields a non-uniform wave velocity in z with the wave amphidromic point (or the point in the vertical at which the horizontal velocity changes sign) at about the maximum topographic height of the canyon. With our constant stratification, this amphidromic point is shifted to half depth, which is the maximum height of our topography and thus in broad agreement with reality. Both this order of magnitude of stratification and the relative constancy of stratification through the water column is observed at the mouth of La Jolla Canyon (Hamann, personal communication). Given that stratification is constant, waves cannot achieve both subcritical and supercritical reflection off the bottom of our V-shaped topography, and thus cannot form a true wave trap, although multiple reflections are still possible with the wave potentially breaking after such reflections (Maas et al., 1997).

Given the small scales of overturning we use a stretched grid to concentrate most of the resolution at the topography and use the coarsest resolution possible away from the topography to resolve the incoming wave. Such a setup allows us to complete an ensemble of simulations while minimizing the computing costs. In the low resolution model runs, Δx varies from 77 to 3 m, Δy is a constant 44 m and Δz is a constant 4 m (corresponding to a grid size of $850 \times 100 \times 50$). The high resolution simulations have Δx varying from 78 to 2 m, Δy varying from 41 to 2 m and Δz a constant 2 m (corresponding to a grid size of $1700 \times 200 \times 100$, exactly double that of the low resolution simulations). At the variable canyon topography, all grid boxes are $2 \text{ m} \times 2 \text{ m} \times 2 \text{ m}$. The turbulent overturning length scales that we aim to capture in the canyon can be characterized by the Ozmidov scale, which is given as $L_O = \sqrt{\epsilon/N^3}$, where ϵ is the turbulent dissipation rate. Using an elevated level of turbulent dissipation of $10^{-6} \text{ m}^2/\text{s}^3$, which is the average maximum dissipation rate seen throughout our suite of canyon simulations, we arrive at an Ozmidov scale of approximately 32 m, which both high and low resolution simulations resolve in the canyon region. Since canyons are symmetric and we do not consider rotation (i.e. $f = 0$), we could have placed a free-slip wall in the center of the canyon, at $y = 0$, to conduct the simulations with half the number of grid points. We choose not to take this approach so that the model configuration is generalizable for future simulations with realistic, non-symmetric canyon topography and rotational effects ($f > 0$).

Low resolution experiments are hydrostatic, while high resolution experiments are conducted using the MITgcm non-hydrostatic capabilities. Since the high resolution simulations begin to resolve the lengthscales of overturning, it is appropriate to turn on the non-hydrostatic capability as mixing is fundamentally a non-hydrostatic process. A comparison of the hydrostatic and non-hydrostatic results is presented in Section 5. A final difference between the low resolution and high resolution simulations is the forced wave velocity amplitude. In the low resolution cases, this amplitude is 2 cm/s, while it is 1.2 cm/s in the high resolution cases. This slight modification was done to make the already costly high resolution simulations more efficient while satisfying the CFL criterion (i.e. $u_{\max} \frac{\Delta t}{\Delta x_{\min}} < 1$ where u_{\max} is the maximum flow speed). Low resolution simulations at this decreased forcing frequency were also conducted to test whether any differences between low and high resolution simulations are amplitude dependent

or dependent on the higher resolution and non-hydrostatic configuration. See Figs. 2 and 3 for density snapshots along the center of the domain from two of the high resolution simulations. The initial Froude number, Fr_0 is 0.32 for the low resolution simulations and 0.19 for the high resolution simulations, safely under the threshold of unity indicating stable initial flow and linear waves. Both low and high resolution simulations have a time step of 1 s, a horizontal kinematic viscosity of $10^{-2} \text{ m}^2/\text{s}$ and a vertical kinematic viscosity of $10^{-3} \text{ m}^2/\text{s}$. The value of scalar diffusivity is set to zero and no turbulence model is used. A one-step, seventh-order monotonicity preserving advection scheme is used, which minimizes numerical diffusion.

In order to reach a quasi-steady state, all simulations are run for 8.5 days. It takes the first 4 days of the simulations for the waves to reach the topography and begin to reflect and refract. Around day 4, the wave energy flux over the canyon and continental shelf attains an approximately constant value, and thus a quasi-steady state is reached. All analysis uses the last 4.5 days (i.e. from tidal cycle seven onwards) to insure all transient effects are omitted.

Three diagnostics are used to analyze the MITgcm numerical simulations. The first two diagnostics are derived (as in Cummins and Oey, 1997; Kurapov et al., 2003; Kang and Fringer, 2012; Buijsman et al., 2012) from the baroclinic energy equation

$$\left\langle \frac{\partial}{\partial t} (KE + APE) \right\rangle + \langle \nabla \cdot \mathbf{F} \rangle = \langle C \rangle - \langle D \rangle - \langle M \rangle \quad (2)$$

where the first term is the tendency of the kinetic and linear available potential energies, the second term is the divergence of the energy flux, the third term is the conversion from barotropic to baroclinic and vice versa, the fourth term is the dissipation and the fifth term is the diapycnal mixing, or residual. The bracket notation indicates that these are tidally averaged quantities. All of these canyon-integrated quantities are shown as a function of the tidal cycle in the MITgcm, in Fig. 4 and inform our assessment of a quasi-steady state being reached at the seventh tidal cycle.

For the first term, the kinetic energy, KE , can be expressed as $\frac{1}{2}\rho_0(u^2 + v^2 + w^2)$ and the linear available potential energy, APE , can be expressed as $g^2\rho'^2/(2\rho_0N^2)$ where ρ_0 is the constant density of 999.8 kg/m^3 , (u', v', w') is the 3D wave velocity field, g is the standard gravitational acceleration of 9.81 m/s^2 and ρ' is the perturbation density, expressed as $\rho'(x, y, z, t) = \rho(x, y, z, t) - \rho_b(z)$, where $\rho_b(z)$ is the background density profile at model initialization. Since the system is in a quasi-steady state, the first term in (2) (i.e. the tendency of the energy) tends to zero, as shown in Fig. 4.

The second term of (2) is the divergence of the energy flux. Given that there is no barotropic flow, this flux can be cast as

$$\mathbf{F} = \mathbf{u}'p' + \mathbf{u}'KE + \mathbf{u}'APE - \mu_H \nabla KE \quad (3)$$

where p' is the pressure anomaly associated with the wave and μ_H is the model's horizontal viscosity (a constant value of $0.01 \text{ m}^2/\text{s}$). There is no explicit contribution from the gradient of the available potential energy, as both the horizontal and vertical components of diffusion are set to be a constant value of 0 in the model. Thus, the flux is composed of three main contributions: pressure work (the first term in (3)), the advection of energy (the second and third terms in (3)) and horizontal diffusion (the fourth term in (3)).

Energy conversion, the third term in (2) can be expressed as

$$C = p'_{-H}W \quad (4)$$

where p'_{-H} is the pressure evaluated at the topography and W is the vertical barotropic velocity (i.e. $W = -\mathbf{U} \cdot \nabla H$, with \mathbf{U} being the horizontal component of the barotropic flow). For our case of remotely generated internal waves, C is a sink term, and found to be small (again see Fig. 4).

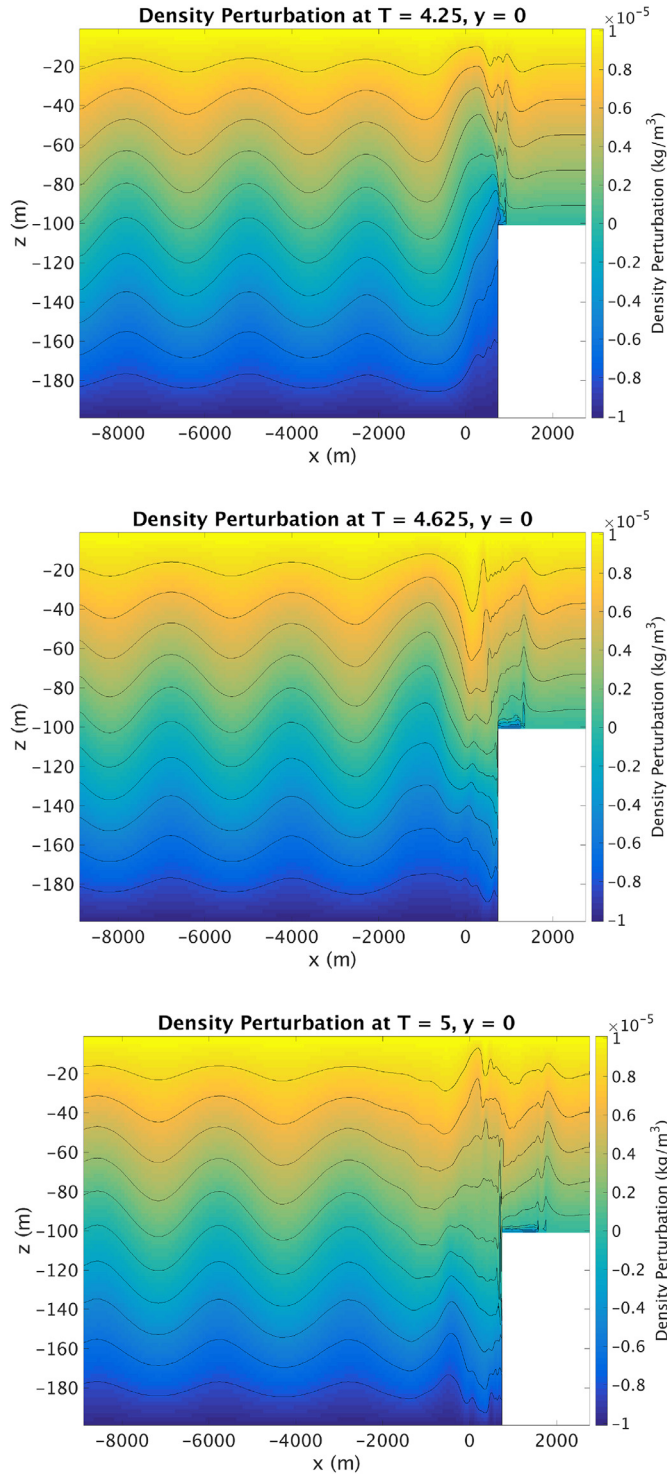


Fig. 3. Instantaneous snapshots of the density perturbation taken along the center of a flat bottom slope canyon with $\zeta = 30^\circ$, taken at three equally spaced intervals over one tidal cycle (T): at (top) 4.25, (middle) 4.625 and (bottom) 5 tidal cycles, respectively. The wave propagates into the domain from the Western boundary, interacts with the topography and is allowed to radiate freely out through the Eastern boundary (x and y are aligned with longitude and latitude, respectively). As seen in the progression of the density field, the wave can also partially reflect back towards the Western boundary. Snapshots taken from the high-resolution simulation. (For interpretation of the references to color in this figure legend, the reader is referred to the web version of this article.)

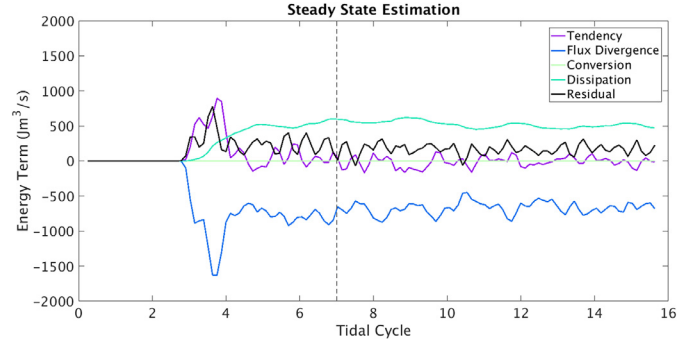


Fig. 4. All terms in energy budget, (2), respectively, using MITgcm model output integrated over the canyon volume for a near-critical slope canyon of $\zeta = 35.9^\circ$. Note that a quasi-steady state (the point at which the tendency term becomes small compared to other terms) is reached around the seventh tidal cycle (dashed line) and all calculations are taken from tidal cycle seven to tidal cycle sixteen. The residual term is calculated as the sum of the tendency, flux divergence and dissipation minus conversion so that Eq. (2) is satisfied. Thus, diapycnal mixing is not explicitly calculated. All terms are calculated as a moving average over one tidal period. (For interpretation of the references to color in this figure legend, the reader is referred to the web version of this article.)

Following the derivation of Kurapov et al. (2003) and the notation of Buijsman et al. (2012), dissipation, the fourth term in (2) can be expressed as

$$D = \rho_0 \left\{ \mu_H \left(\left[\frac{\partial \mathbf{u}'}{\partial x} \right]^2 + \left[\frac{\partial \mathbf{u}'}{\partial y} \right]^2 \right) + \mu_V \left[\frac{\partial \mathbf{u}'}{\partial z} \right]^2 \right\} \quad (5)$$

where μ_V is the vertical viscosity, set to a constant of $0.001 \text{ m}^2/\text{s}$. For both the energy flux, (3), and dissipation, (5), the vertical velocity perturbation, w' is omitted from the hydrostatic simulation diagnostics and is included in diagnostics for the nonhydrostatic simulations. The fifth term in (2) is the diapycnal mixing term and is very difficult to accurately capture through model diagnostics. Given that it is a small contribution to the overall energy budget, it is evaluated as a residual (see Fig. 4).

If the tendency, conversion and diapycnal mixing terms (i.e. $\partial/\partial t$, C and M , respectively) are small, then for a remotely generated internal wave with no background, barotropic flow, (2) reduces to

$$\langle \nabla \cdot \mathbf{F} \rangle = -\langle D \rangle + K \quad (6)$$

where K is the residual term, resulting from any small energy conversion from the baroclinic to the barotropic, any small deviation of the energy tendency in the tidal average, a small contribution from diapycnal mixing and numerical dissipation as well as any small errors related to conducting these calculations offline (Buijsman et al., 2012). We then take a volume integral of (6) over the canyon region and, after applying Gauss' Theorem, obtain

$$\iint_{S(V)} \langle \mathbf{F} \rangle \cdot \hat{\mathbf{n}} \, dS = - \iiint_V \langle D \rangle \, dV + \mathcal{K} \quad (7)$$

where V is the canyon volume, $S(V)$ are the surfaces, or faces, of that canyon volume and \mathcal{K} is the volume-integrated residual. This equality provides the setup for calculating our first two diagnostic quantities, which we refer to as E_1 and E_2 .

E_1 is the left-hand side of (7). Based on our model configuration, we calculate this as

$$E_1 = \left\langle \left\{ \left[\int_H \int_{(d-c)} F_x \, dy \, dz \right]_a^b - \left[\int_H \int_{(b-a)} F_y \, dx \, dz \right]_c^d \right\} \right\rangle \quad (8)$$

where F_x and F_y are the x - and y -components of the energy flux (3), respectively, H is the topographic depth, a corresponds to the face before the canyon mouth (open ocean), b corresponds to the

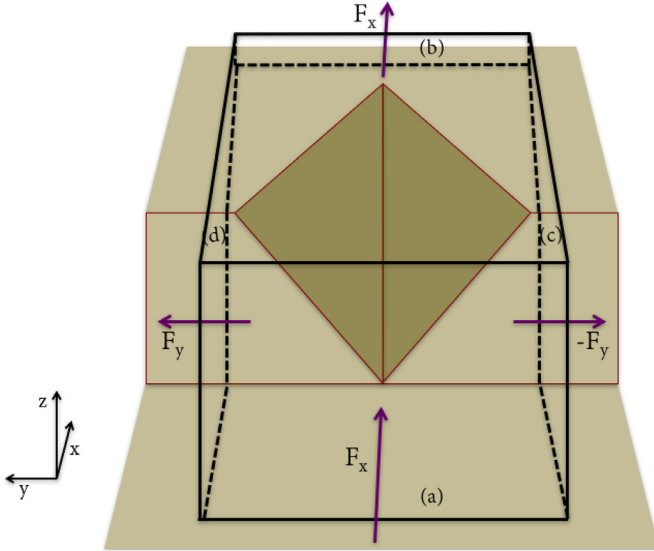


Fig. 5. Schematic of the region over which the volume-integrated divergence of the energy flux, E_1 , is calculated for all simulations. The divergence of the energy flux is the difference between the incoming flux normal to the mouth of the canyon and the flux out of the canyon. Note that the faces a , b , c and d are the same bounds used to calculate the volume-integrated dissipation, E_2 . (For interpretation of the references to color in this figure legend, the reader is referred to the web version of this article.)

face after the canyon head (continental shelf), c corresponds to the face flanking the Southern-most point of the canyon and d corresponds to the face flanking the Northern-most point of the canyon (see Fig. 5 for a schematic of this setup). Faces c and d are taken at the edge of the canyon, while faces a and b are taken just before and after the canyon, respectively, to include all canyon-induced energy loss. This x -extent of energy loss due to the canyon will be further discussed in Section 4. Thus, the divergence of the energy flux, E_1 , is the difference between the energy flux leaving the canyon region (primarily through faces b , c and d , with some backwards reflection also occurring through face a) and the energy flux initially entering the canyon region through face a . Inward and outward energy fluxes through face a are not calculated separately, rather the net flux at a is calculated with the directionality of the flux being determined by the sign of the zonal velocity.

The second diagnostic, E_2 , is the dissipation, which is present on the right-hand side of (7). Based on our model setup, the volume integral of dissipation in (7) can be rewritten with the proper boundaries as

$$E_2 = \left\langle \int_H \int_{(d-c)} \int_{(b-a)} \left\{ \mu_H \left[\left(\frac{\partial \mathbf{u}'}{\partial x} \right)^2 + \left(\frac{\partial \mathbf{u}'}{\partial y} \right)^2 \right] + \mu_V \left(\frac{\partial \mathbf{u}'}{\partial z} \right)^2 \right\} dx dy dz \right\rangle \quad (9)$$

Recall that, for the hydrostatic simulations, the w' term in both (8) and (9) is omitted. Both E_1 and E_2 have 8 outputs per tidal cycle (12 hours) and are both averaged over each cycle to remove the tidal variability. There are thus 9 different E_1 and E_2 values per experiment. These values are again averaged to obtain \bar{E}_1 and \bar{E}_2 , with associated errors quantified by calculating the standard deviation of the mean.

In the ray tracing model, we calculate the Froude number using the velocity associated with the wave. However, in MITgcm simulations, the wave component cannot be differentiated from other motion, so the wave Froude number cannot be determined in these simulations. Instead we use the Richardson number, which is not

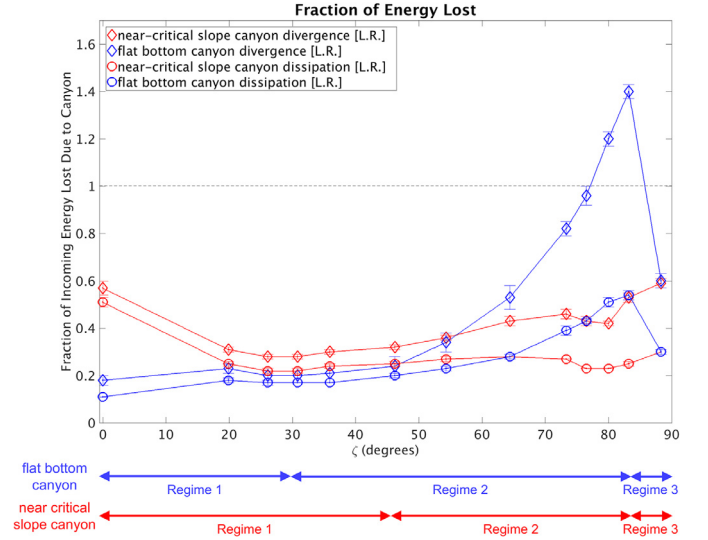


Fig. 6. Fraction of incoming wave energy dissipated in the canyon region. Also included are the near-critical slope and vertical wall controls, marked at $\zeta = 0^\circ$. (For interpretation of the references to color in this figure legend, the reader is referred to the web version of this article.)

particular to the wave, as the third and final diagnostic for the numerical model.

The Richardson number is the ratio of the stratification to the square of the shear. Mathematically, it can be cast as

$$Ri = \frac{N^2}{S^2} \quad (10)$$

where $S^2 = (\partial \mathbf{u}'_H / \partial z \cdot \partial \mathbf{u}'_H / \partial z)$ and \mathbf{u}'_H is the horizontal component of wave velocity, (u', v') , which is easily calculated for all stratifications, including statically unstable scenarios. By the Miles–Howard criterion, linear stability of parallel shear flow requires $Ri > 1/4$; below this Richardson number the destabilizing effect of shear can overcome the stabilizing effect of stratification (Yih, 1980). Our scenario is not one of parallel shear flow, and this value of critical Richardson number is not generally applicable for all flows (Galperin et al., 2007; Lamb and Farmer, 2011); nonetheless, we will use $Ri < 1/4$ as a guide to regions where instability is more likely. The spatial structure of the simulation's minimum Richardson number and turbulent dissipation nicely align. This agreement is not an artifact of the model, as there is no sub-grid scale scheme linking Richardson number and dissipation. Thus, despite the studies illustrating variations of the Richardson number threshold for instability, the canonical value of $1/4$ appears appropriate for our study.

While we broadly expect the Richardson number in the model to be small in the same regions where the Froude number is large from the ray tracing, we may not expect a perfect match. Due to the fact that the output from the MITgcm is for the total fluid flow, and that the Froude number is implicitly a wave quantity, it is more appropriate to use the Richardson number to understand regimes of instability from the MITgcm output. Conversely, the Froude number is more appropriate to gain insight into the regimes of instability in the ray tracing algorithm since we are only considering the wave field. Additionally, the ray tracing only uses a constant stratification, whereas the stratification in the model can change in the presence of the internal wave, thus altering the Richardson number. Despite the differences, both quantities are the most appropriate way to diagnose the potential instability in each of the two different methodologies.

In Section 4, \bar{E}_1 , \bar{E}_2 and Ri will be used to quantify the wave breaking in the MITgcm and Fr , the Froude number, as well as its

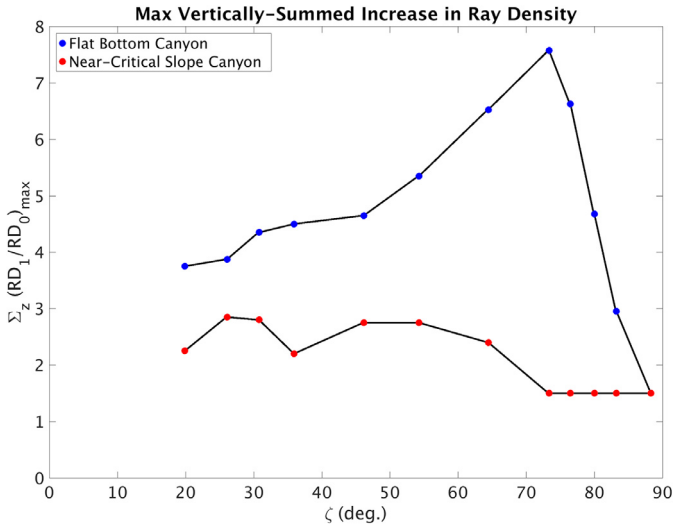


Fig. 7. The maximum vertically summed increase in ray density as a function of the canyon width for flat bottom canyons (blue) and near-critical slope canyons (red). Dots indicate the values calculated for each value of ζ used in the canyon simulation. The relative maximum value for the flat bottom canyon occurs at $\zeta = 73.3^\circ$ and the relative maximum for the near-critical slope canyon occurs at $\zeta = 26.1^\circ$ (For interpretation of the references to color in this figure legend, the reader is referred to the web version of this article.)

component pieces of RD and m , ray density and vertical wavenumber, respectively, to quantify potential instability in the ray tracing algorithm (for a full discussion of the Froude number, ray density and vertical wavenumber, please see Part 1 of this study, Nazarian and Legg (2017a)).

4. Results

We start with a presentation of the MITgcm results and use the ray tracing algorithm that we have developed to interpret the results. Conversely, we use the MITgcm results to verify that the linear ray tracing algorithm is a useful method for understanding the internal wave scattering problem in continental slope canyons.

In order to study the relative enhancement of wave breaking and wave-driven mixing due to the canyons, we normalize the values of \bar{E}_1 and \bar{E}_2 by the total energy being fluxed into the canyon region through the Western face (i.e. face a). The energy flux into the canyon is calculated using a flat control simulation, so this incoming energy flux is not affected by any topographic reflection. That is, we run a control simulation in which the topography is flat, and has a depth equal to the maximum depth present in the canyon simulations. This allows us to diagnose the incoming tidally-averaged wave flux without interference from reflected and refracted waves. The results for \bar{E}_1 and \bar{E}_2 are presented in Fig. 6. In addition to the fraction of the energy lost in each of the canyons, Fig. 6 includes the fractional energy loss for two control simulations; a near-critical slope (same criticality as the near-critical slope canyon thalweg) and a vertical wall (both denoted at $\zeta = 0^\circ$). There are three main regimes in the fractional energy loss. In Regime 1, both classes of canyons maintain a relatively constant energy loss as ζ increases. Recall that this corresponds to a decrease in the canyon mouth width. Fig. 6 also illustrates another region we deem Regime 2, in which the fractional energy loss increases with increasing (decreasing) ζ (canyon width), albeit with a slight dip in the energy loss for near-critical slope canyons around $\zeta = 80^\circ$. Finally, we have Regime 3 in which the fractional energy loss decreases for the flat-bottom canyons and increases slightly for the near-critical slope canyons with increasing ζ . The regime threshold of $\zeta = 83^\circ$ is taken empirically from the model simulations. The analysis of the differences between the divergence

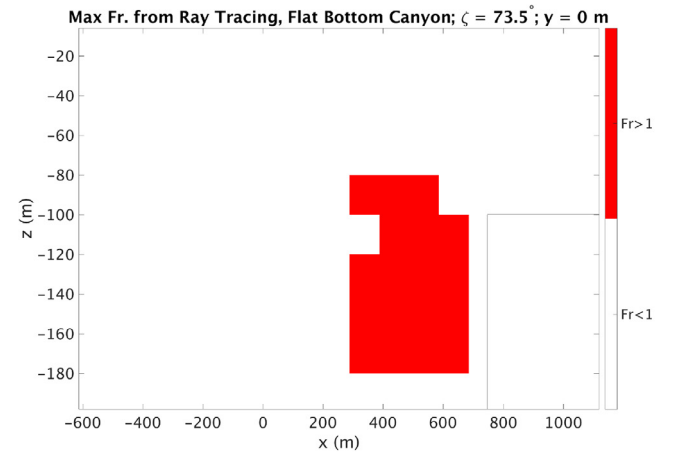
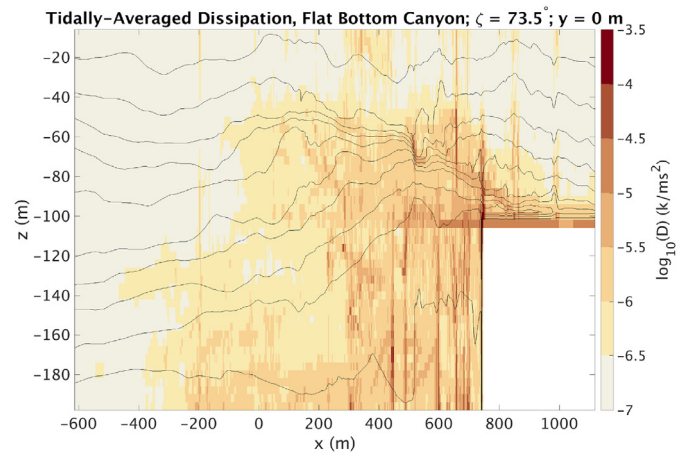
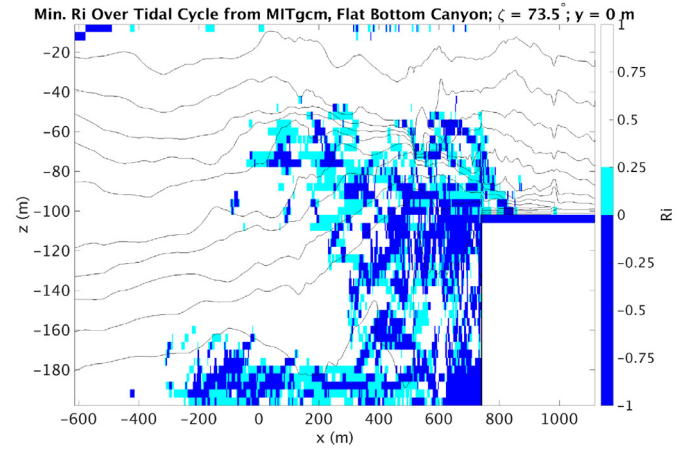


Fig. 8. (Top) Minimum Richardson number for one tidal cycle and (middle) tidally averaged dissipation in the low-resolution, hydrostatic MITgcm simulation and (bottom) maximum Froude number from the ray tracing algorithm, taken along the center of a flat bottom canyon in the second regime. (Top) By the Miles–Howard criterion, all cyan regions can experience shear instability while navy regions additionally can experience convective instability. (Middle) There is generally good agreement between the regions of enhanced dissipation and Richardson number. Isopycnals (black lines) are drawn for reference and taken as a snapshot at $T = 10$ tidal cycles. (Bottom) Regions in which the Froude number is larger than unity are regions where instability can develop. Note that the canyon mouth is located at $x = 0$ m. (For interpretation of the references to color in this figure legend, the reader is referred to the web version of this article.)

of the energy flux and the dissipation, as well as the occurrence of fractional energy losses greater than one, are left for Section 5.

We first investigate the case of the flat bottom canyon. From the ray tracing (Part 1), we know that for the first regime there is, at most, one ray reflection inside the canyon. Thus, these canyons are not efficient at trapping wave energy and causing the wave to break. This lack of wave focusing aligns with the results from Fig. 6 that there is only a moderate increase in the fraction of energy loss in these canyons versus the vertical wall control (i.e. $\zeta = 0^\circ$). As ζ increases towards the threshold of 30° , fewer rays are able to enter the canyon region due to the narrowing canyon mouth, which leads to the relatively steady fraction of energy loss. In addition to the intuition gained from the ray tracing, this process is coupled with mixing that takes place at the canyon lip, similar to the case at a vertical wall or knife-edge (Klymak et al., 2013) (we illustrate this boundary mixing later, in Fig. 8). By incising a canyon into a vertical wall, we essentially extend the length of the vertical wall, thereby extending the length over which boundary mixing can occur. Thus, there is a moderate increase in the energy lost in these canyons compared to a homogeneous vertical wall, as wave focusing toward the canyon center can function as an additional process leading to mixing.

We now consider the second regime ($30^\circ < \zeta < 83^\circ$) for the case of the flat bottom canyon. Note that subsequent ray reflections inside the canyon are now possible and, at $\zeta = 45^\circ$, the second reflection must be further into the canyon. This is in contrast to the outward reflection of rays that characterizes the first regime. The magnitude of relative ray density per grid box is slightly enhanced in this regime, compared to the first regime (this aligns with an increase in ray density observed in the ray tracing in Paper 1). Once the ray density is increased sufficiently (and the Richardson number is therefore reduced sufficiently), the wave breaks and overturning occurs, thereby leading to dissipation and mixing. The third regime occurs for $\zeta > 83^\circ$, and this regime is characterized by a noticeable decrease in energy loss. While the ray tracing from Part 1 illustrates that these narrow canyons can lead to many ray reflections, there are few rays that are able to propagate into these canyons and so the ray density increase, and thus instability, decreases sharply.

We can gain further insight into the spatial patterns of dissipation and mixing by considering the Richardson number diagnosed from the MITgcm simulations. Fig. 8 illustrates the minimum Richardson number over one tidal cycle, as well as the maximum Froude number diagnosed from the ray tracing, along the center of a flat bottom canyon in the second regime of ζ -space, close to the maximum in relative energy loss. The tidally averaged dissipation is also included in Fig. 8 to show the agreement between the spatial pattern of turbulent dissipation and regions of instability taken from the Richardson and Froude number calculations. For both nondimensional numbers, shaded regions designate regions where instabilities are possible. According to the Kelvin–Helmholtz criterion for instability, there are many regions in this case of flat bottom canyon which are potentially unstable. Specifically, the Richardson number calculation points to turbulent boundary layers emanating from the lip of the canyon towards the ocean interior. Fig. 8 has a region of instability up to 40 m high and 500 m laterally. This region emanating away from the canyon lip is a region of overturns due to an arrested lee wave, similar to that seen in Klymak et al. (2013). This type of instability cannot be predicted from the linear ray density metric. Furthermore, Fig. 9 presents instantaneous turbulent dissipation along the center of the canyon, taken at three instances during the same tidal cycle that the average is taken over. Tidal variation in dissipation along the center of the canyon is pronounced and extends much further away from the slope than that observed for a homogenous vertical wall.

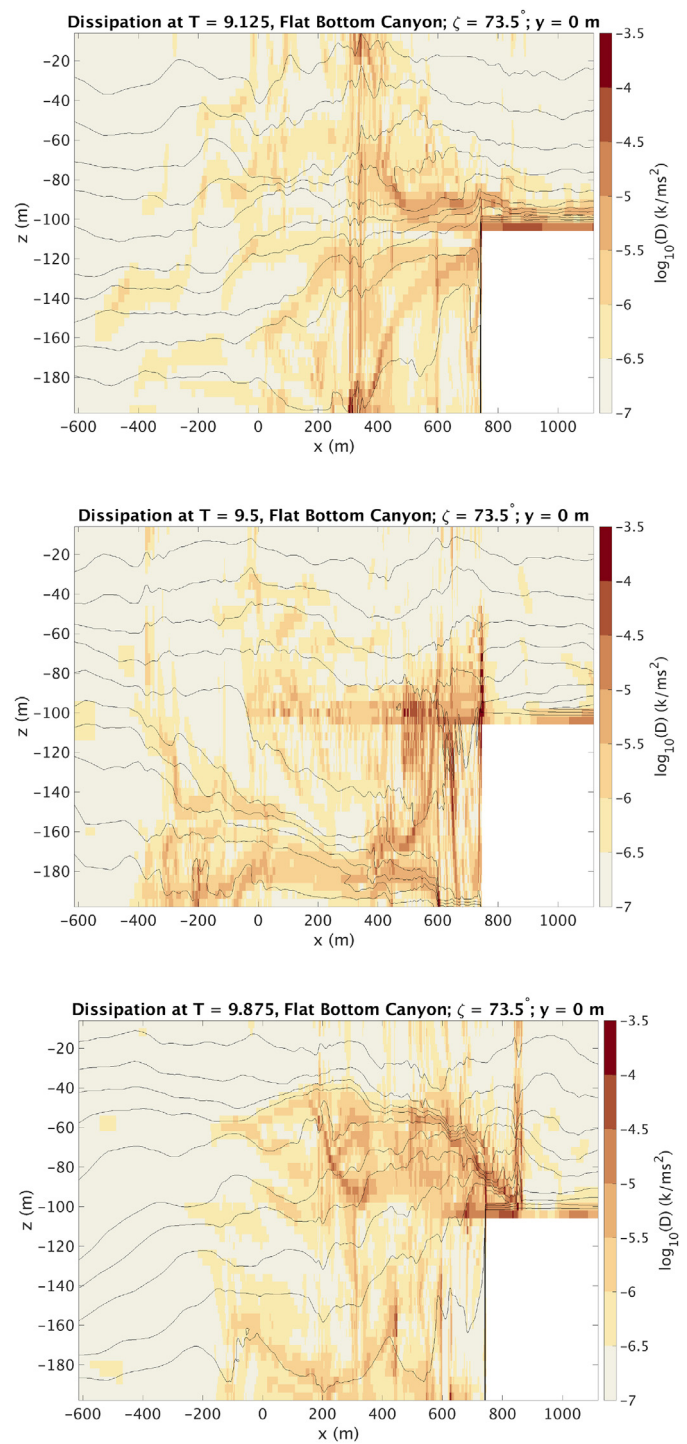


Fig. 9. Instantaneous turbulent dissipation along the center of a narrow ($\zeta = 73.5^\circ$) flat bottom canyon at three instances during one tidal cycle, each separated by approximately a third of a tidal cycle: (top) 9.125 tidal cycles, (middle) 9.5 tidal cycles and (bottom) 9.875 tidal cycles. Instantaneous isopycnals are drawn in black. Note that the canyon mouth is located at $x = 0$ m. (For interpretation of the references to color in this figure legend, the reader is referred to the web version of this article.)

Although there are some regions where mixing occurs which are not predicted from the ray tracing model, indicating non-linear processes are occurring, Fig. 8 illustrates that there is a generally good agreement between the spatial pattern of the minimum Richardson number and the maximum Froude number from ray tracing. For instance, we observe that there is the potential for instability extending away from the canyon head along the sea

floor (between $x = 0$ m and $x = 500$ m) which has not been observed before for plain vertical walls. Instead, this instability is the result of wave reflection in the canyon region and the resulting convergence of rays along the center of the canyon. This region of instability also increases as ζ increases further into Regime 2. This relatively good match is an example of the utility of the ray tracing. Although it cannot capture the presence of the nonlinear lee wave, on the whole it matches the envelope of instability as diagnosed from the Richardson number in the numerical simulations reasonably well. Despite its limitations, the ray tracing model may be a useful tool to understand and predict parameter regimes in which increased energy loss is possible.

The transition to the third regime, which we estimate from the MITgcm parameter space sweep to be 83° , is empirically determined. We now attempt to use the theory that we have developed to explain this threshold. The physical argument that has been employed to describe the drop off in energy loss for very narrow canyons is that, while they are efficient dissipators, very little energy can enter through the narrow canyon mouth. We find the maximum vertically-summed increase in ray density, $(\sum_z (RD_1/RD_0))_{\max}$ in the canyon region as a function of parameter ζ by running the ray tracing algorithm for each simulation (see Fig. 7). The maximum value of the wave focusing efficiency occurs at $\zeta = 73.3^\circ$ in the ray tracing data. Not only is this close to the transition point seen in the MITgcm simulations, but furthermore, Fig. 7 closely resembles the behavior of the energy loss diagnostics as a function of ζ seen in Fig. 6. This analytical approximation thus qualitatively captures the transition from the second to third regime, giving support to our theory for the physics leading to this transition, as well as confirming the utility of the ray tracing algorithm.

While the majority of the attention has been given to the flat bottom canyon, the near-critical slope canyon case behaves similarly. The main distinction between the near-critical slope canyon and flat bottom canyon is that the sidewalls are not vertical in the case of the near-critical slope canyon, which allows a change/redistribution of wavenumber upon reflection, as outlined in Part 1. The main implication of this physics is that, in the first regime ($\zeta < 30^\circ$), the rays are still scattered out of the canyon upon reflection, but onto the shelf, leading to relatively little energy loss in this regime. Given that the homogeneous critical slope is such an efficient dissipator of internal waves, it comes as no surprise that these relatively wide canyons are less efficient wave dissipators. Unlike the flat bottom canyon case, the transition between the first regime of outward scattering and the second regime of secondary reflections for critical slope canyons no longer occurs at $\zeta = 30^\circ$ (i.e. the relative energy loss for the near-critical slope canyons around 30° are relatively constant). Instead, the transition point is shifted to $\zeta = 45.3^\circ$ (as shown in Part 1). The offset between this regime-two transition point and that of the flat bottom canyon is a result of the difference in sidewall steepness. While the point of transition is shifted, the second regime still has the same underlying physics; rays are now reflected back into the canyon region where they can further reflect and scatter. As the number of reflections increases, so too does the likelihood of increasing vertical wavenumber and breaking. Note however that there is decrease in the relative energy loss centered around 80° that is not observed for the flat bottom canyons. This is due to the fact that the ray density in the near-critical slope canyons decreases earlier as a function of ζ .

Finally, the third regime occurs at the same threshold as for the flat bottom canyon ($\zeta = 83^\circ$, again empirically defined), but now the energy loss has a modest increase with increasing ζ . Although the ray density decreases rapidly, the increase in vertical wavenumber increases to a greater extent around this threshold from Regime 2 to 3, thus leading to a slight uptick in relative en-

ergy losses. We repeat the approach of taking the maximum vertically summed increase in ray density for the near-critical slope canyon (seen in Fig. 7), however the agreement with the MITgcm relative energy loss (Fig. 6) is not as good for the case of the flat bottom canyon. This confirms our understanding that it is not only the change in ray and energy density in the near-critical slope canyons that leads to instability, but additionally the increase in vertical wavenumber, which has a stronger effect for larger values of ζ (see Part 1).

We show the minimum Richardson number over one tidal cycle along the center of a Regime Two near-critical slope canyon in Fig. 10. Like a plain near-critical uniform slope, we notice a broad region of shear instability along the slope with pockets of convective instability. As has been shown in the literature, this is due to a near-critical reflection and the subsequent high density of rays and energy along the slope (Ivey and Nokes, 1989). Fig. 10 differs from a plane near-critical slope in that regions of potential instability extend away from the slope (i.e. $x < 0$). As in the case of the flat bottom canyon, we attribute this instability away from the canyon as a direct result of ray scattering and focusing within the canyon region, which increases the ray density along the center of the canyon. We again calculate the maximum Froude number from the ray tracing algorithm, seen in the bottom panel of Fig. 10. Thus, from taking the Froude and Richardson numbers in tandem, we see that the energy loss in the canyon region is the cumulative result of increased vertical wave number, as well as increased ray density. Again, note the agreement between the linear theory (ray tracing) and the numerical simulation.

In addition to a match between the regions of instability diagnosed from the nondimensional numbers, Fr and Ri , the spatial patterns of instability match the spatial patterns of tidally averaged turbulent dissipation calculated from the MITgcm (Fig. 10). This suggests that these nondimensional numbers are useful in understanding the energy loss within the canyon and serves as another demonstration that the internal wave scattering dynamics within canyons can be understood and predicted through the ray tracing algorithm that we have developed. Furthermore, Fig. 11 presents instantaneous turbulent dissipation along the center of the canyon, taken at three instances during the same tidal cycle that the average is taken over. Tidal variation in dissipation along the center of the canyon is pronounced. We attribute this variation to a nonlinear bolus sloshing up the canyon. Note, however, that for all three snapshots in Fig. 11, the envelope of dissipation extends much further away from the slope than that observed for a homogenous critical slope.

So far, all calculations of energy loss, both \bar{E}_1 and \bar{E}_2 , have been considered relative to the total energy flux entering the canyon region. To adequately determine whether canyons are more efficient at dissipating internal wave energy than their sloping counterpart, we normalize both \bar{E}_1 and \bar{E}_2 by the energy loss over a control topography of the same width (specifically, \bar{E}_1 for the canyon is normalized by \bar{E}_1 for the control and likewise \bar{E}_2 for the canyon is normalized by \bar{E}_2 for the control). Thus, we normalize all of the near-critical slope canyon calculations of energy loss by the energy loss over a near-critical slope (i.e. the same slope as the canyon thalweg) of the same width and height. Similarly, we normalize all flat bottom canyon energy loss calculations by the energy loss occurring over a vertical wall of the same width and height. Although vertical walls are not efficient dissipators of internal wave energy, we construct this control to tease out the effect of wave focusing by the canyon. Results are shown in Fig. 12.

There are two main results that can be drawn from Fig. 12. First, note that the ratio of the energy loss in the near-critical slope canyon relative to the energy lost over a planar near-critical slope is less than or approximately unity throughout the ζ parameter space. For smaller values of ζ , this ratio is significantly

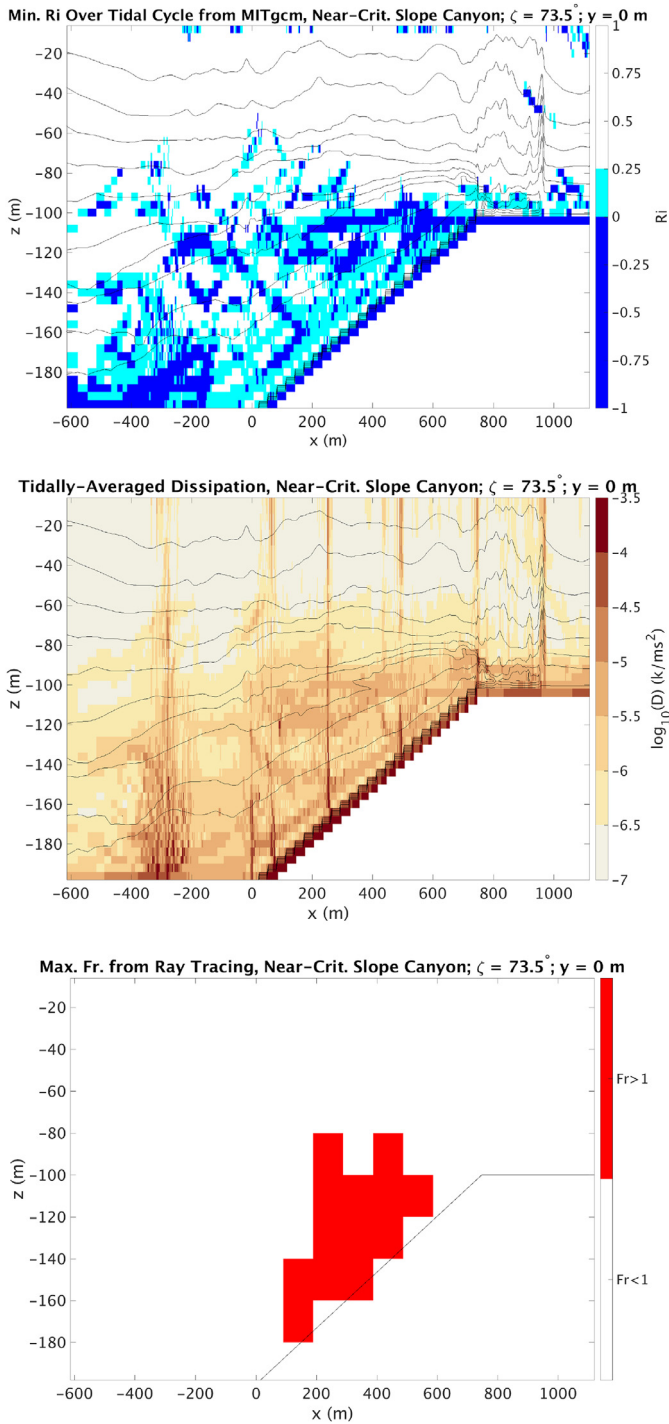


Fig. 10. (Top) Minimum Richardson number for one tidal cycle and (middle) tidally averaged dissipation in the low-resolution, hydrostatic MITgcm simulation and (bottom) maximum Froude number from the ray tracing algorithm, taken along the center of a near-critical slope canyon in the second regime. (Top) By the Miles–Howard criterion, all cyan regions can experience shear instability while navy regions additionally can experience convective instability. (Middle) There is generally good agreement between the regions of enhanced dissipation and Richardson number. Isopycnals (black lines) are drawn for reference and taken as a snapshot at $T = 10$ tidal cycles. (Bottom) Regions in which the Froude number is larger than unity are regions where instability can develop. Note that the canyon mouth is located at $x = 0$ m. (For interpretation of the references to color in this figure legend, the reader is referred to the web version of this article.)

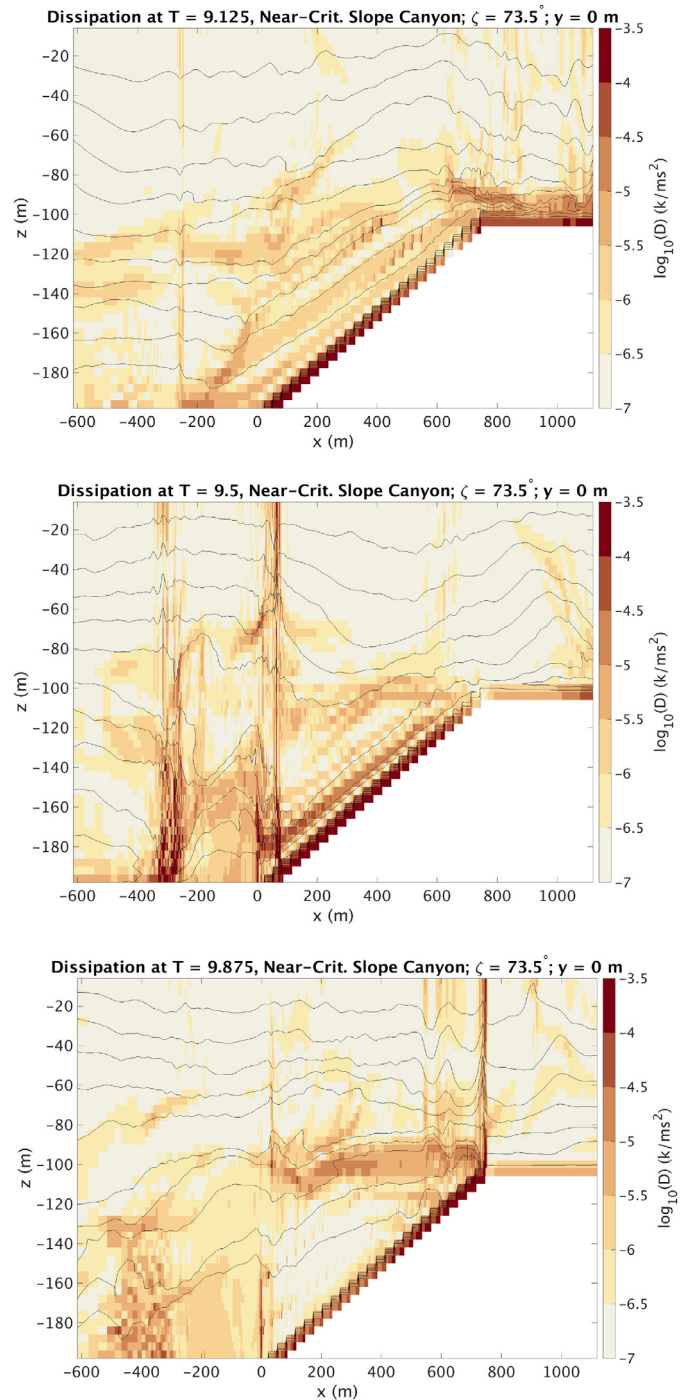


Fig. 11. Instantaneous turbulent dissipation along the center of a narrow ($\zeta = 73.5^\circ$) near-critical slope canyon at three instances during one tidal cycle, each separated by approximately a third of a tidal cycle: (top) 9.125 tidal cycles, (middle) 9.5 tidal cycles and (bottom) 9.875 tidal cycles. Instantaneous isopycnals are drawn in black. Note that the canyon mouth is located at $x = 0$ m. (For interpretation of the references to color in this figure legend, the reader is referred to the web version of this article.)

less than one and, as ζ increases, moves toward unity. This behavior can again be explained using the three physical regimes we defined to explain Fig. 6. Specifically, for small ζ values, the canyon dissipates a small amount of energy since rays reflect out of the canyon, while the planar near-critical slope is a very efficient dissipator of energy. The near-critical slope canyon only achieves a near-critical slope along its thalweg, so the wave has less opportunity to undergo a near-critical reflection, and the associated

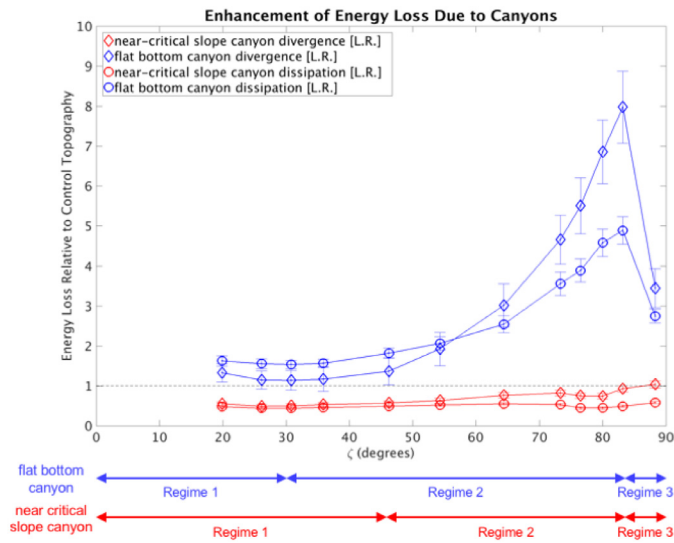


Fig. 12. Ratio of internal wave energy lost in canyon region normalized by the control. For the near-critical slope canyons, the control is a near-critical slope, while for the flat bottom canyons, the control is a vertical wall. Any values greater than unity (indicated with the dashed line) indicate a parameter configuration yielding more energy loss in the canyon than in the corresponding control. (For interpretation of the references to color in this figure legend, the reader is referred to the web version of this article.)

enhanced mixing. As ζ increases, and the second regime is realized, the energy loss in the canyon and energy loss over the planar near-critical slope become more comparable due to wave trapping and the moderate increase in vertical wave number. Relative energy loss remains comparable for the third regime, although these canyons are so narrow that the total energy entering the canyon is small. It is important to note that, regardless of the value of ζ , near-critical slope canyons do not constitute a large increase in energy loss compared to a uniform near-critical continental slope.

The second main result that emerges from Fig. 12 regards the flat bottom canyon. Specifically, for all values of ζ , and thus every regime, the flat bottom canyon dissipates more energy than its analogous vertical wall control. This is mainly a result of the diagnostic we are calculating. Specifically, the vertical wall mainly acts to reflect the wave and only dissipates a small fraction of its energy. Thus, since we divide by a small control, the relative energy loss due to the flat bottom canyon appears strikingly large. Note, however, that the overall fraction of energy loss for the flat bottom canyon seen in Fig. 12 has the same ζ dependence as seen for the flat bottom canyon in Fig. 6, which shows the fraction of incoming energy lost due to the presence of the canyon. Thus, for sections of the continental slope which are steep, the presence of flat bottom canyons poses an opportunity, by up to a factor of eight, to increase energy loss from the wave and the likelihood of diapycnal mixing. This is in good agreement with the ray tracing algorithm, which predicts a factor of eight increase in ray density for relatively narrow flat bottom canyons (Fig. 7), again illustrating the utility of the ray tracing algorithm. This contrasts with the near-critical slope canyon where there is not necessarily more energy loss in the canyon than in the control. This is hinted at in Fig. 6, where both control simulations, the near-critical slope and vertical wall, are plotted at $\zeta = 0^\circ$.

4.1. Resolution dependence

All of the results presented thus far concern the low resolution simulations. We test the resolution dependence of the results by repeating certain canyon geometries in a non-hydrostatic, high res-

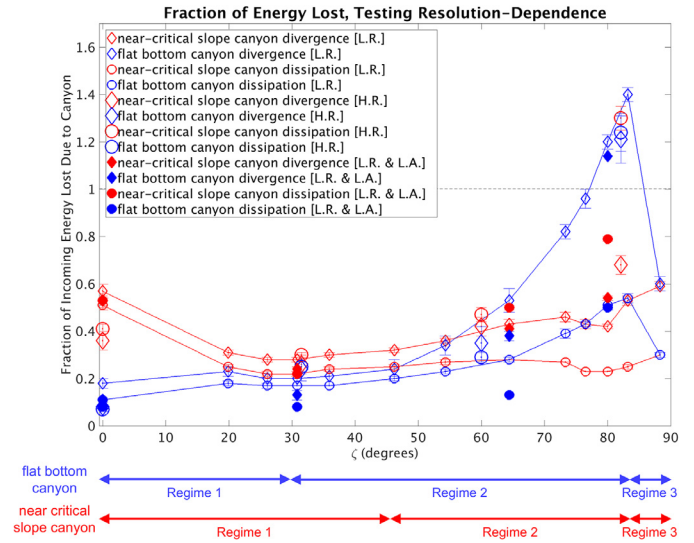


Fig. 13. Same as Fig. 6, now including the high-resolution, low-amplitude simulations and the low-resolution, low-amplitude simulations. Note that L.R. denotes low resolution, H.R. denotes high resolution and L.A. denotes low amplitude. (For interpretation of the references to color in this figure legend, the reader is referred to the web version of this article.)

olution configuration. Results are shown in Fig. 13. There is a small, albeit distinguishable, difference between the low-resolution, hydrostatic simulations and the high-resolution, non-hydrostatic simulations for large ζ . We believe that the high resolution, non-hydrostatic simulations are resolving some of the smaller scale mixing and overturning properties better than the low resolution simulations, such that higher energy dissipation may be achieved. It is important to stress that, since we are conducting a parameter sweep, we are primarily interested in the behavior in ζ and between the two canyon thalweg slopes (α_t), under which we find consistent behavior in both parameters between the low and high resolution suites of simulations.

Additionally, as mentioned in Section 3, the high resolution simulations are conducted with a lower forcing amplitude to satisfy the CFL criterion. Although the metrics for energy loss have a nonlinear dependence on the velocity amplitude, we expect this amplitude-dependence to be modest when dividing by the incoming flux or control, respectively, since these are also taken at the same lower amplitude. Both forcing amplitudes, and thus both incoming Froude numbers, are also the same order of magnitude (0.3 and 0.2 for low and high resolution simulations, respectively) and thus both are safely within the same regime of initial flow stability. To verify this hypothesis, we ran the low-resolution, hydrostatic simulations at the same reduced forcing amplitude as the high resolution simulation. Results are shown in Fig. 13. Note that the change in forcing velocity may account for some of the difference between the low- and high-resolution simulations but, as we conjectured, the result is small as all values are normalized by the control with the same forcing frequency. The same pattern, of relatively little change, is observed when normalizing the energy loss in the canyon relative to the incoming tidal energy.

Finally, for the low resolution, hydrostatic simulations only a few grid cells comprise the canyon in the along-slope direction, which may introduce numerical errors. The small width for very large values of ζ is necessitated by the requirement that the length of the canyon be held fixed for all experiments. However, for large ζ , the high resolution, non-hydrostatic simulations mirror the energy loss patterns of the low resolution, hydrostatic simulations in Fig. 13 giving some confidence in these results despite their coarse resolution.

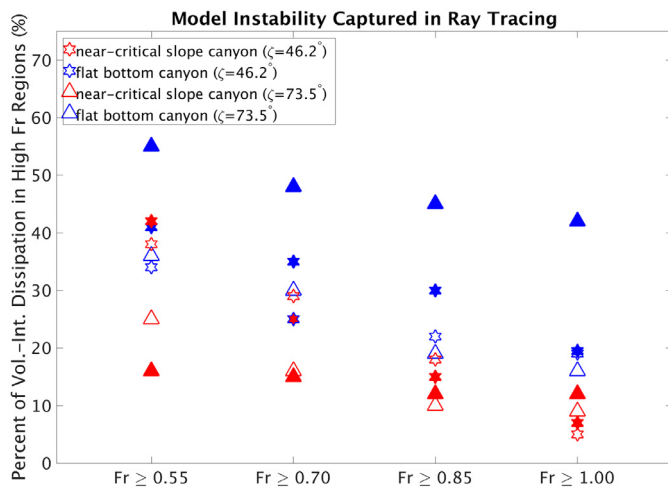


Fig. 14. Percentage of the volume-integrated turbulent dissipation diagnosed that occurs in regions of elevated Froude number as predicted by the ray tracing algorithm. Unfilled markers denote the comparison taken over the entire canyon; filled markers denote the comparison taken along the canyon center (i.e. a cross-section in the x - z plane). This comparison is conducted for four different Froude number thresholds: 0.55, 0.70, 0.85 and the canonical value of 1. (For interpretation of the references to color in this figure legend, the reader is referred to the web version of this article.)

4.2. Ray tracing robustness

We have seen in both Figs. 8 and 10 that there is a relatively good qualitative agreement between the spatial extent of instability predicted by the ray tracing algorithm and the spatial extent of instability diagnosed from the Richardson number and turbulent dissipation in the MITgcm. In all of the ray tracing figures, we have used the canonical threshold of $Fr = 1$ to determine where instability is possible. We now conduct a more quantitative test of the robustness of the ray tracing algorithm for this threshold of $Fr = 1$, as well as for lower Froude number thresholds.

In order to gain a more quantitative understanding of the degree to which the region of potential instability predicted by the Froude number matches the region of turbulent mixing in the model, we consider the volume-integrated turbulent dissipation diagnosed from the MITgcm. Specifically, we take the ratio of the volume-integrated dissipation in the grid boxes where the Froude number predicts instability and the volume-integrated dissipation over the entire canyon. Results are plotted in Fig. 14, and denoted by the unfilled markers. For the canonical Froude number threshold of unity, plotted on the right of Fig. 14, the linear ray tracing captures about 5–15% of the dissipation, depending on the canyon thalweg slope and the canyon aspect ratio (ζ). Overall, the ray tracing algorithm better captures the instability for the flat bottom canyons than the near-critical slope canyons. We additionally consider just the canyon center (i.e. a cross-section along the canyon center in the x - z plane), which is plotted in Fig. 14 in the form of filled markers. The ray tracing does a significantly better job in capturing the instability along the canyon center than over the entire canyon. This is unsurprising, given the relatively good agreement in the spatial maps of instability presented in Figs. 8 and 10.

We repeat this test three more times, each with a successively lower Froude number threshold, and present the results in Fig. 14. As the Froude number threshold is lowered, the ray tracing algorithm's region of instability more closely matches the MITgcm and thus encompasses more of the turbulent dissipation. For the lowest threshold, $Fr \geq 0.55$, the ray tracing algorithm captures approximately 30–55% of the dissipation for the flat bottom canyons, and approximately 15–42% of the dissipation for the near-critical slope

canyons. The increase in instability captured by the ray tracing for lower Froude number thresholds is present when considering both the entire canyon, as well as slices taken down the center of the canyon.

As mentioned briefly in Part 1, there are regions of instability that the ray tracing algorithm can never predict, and thus we can never attain 100% of the model's dissipation in Fig. 14. There are regions of strongly nonlinear processes, namely bores and arrested lee waves, which can never be encapsulated in a linear context. Additionally, we can not predict regions of constructive and destructive interference from the ray tracing algorithm. Given the focusing effects of canyons, constructive interference, and the subsequent wave steepening and breaking, could account for part of the dissipation mismatch between the ray tracing and MITgcm. Despite these limitations, particularly in not being able to diagnose constructive and destructive interference, the ray tracing model has still been shown to be a useful tool to understand and predict parameter regimes in which increased energy loss is possible (particularly in the context of Fig. 7).

It is also imperative to note that the Froude number threshold of 1 for instability is a threshold for supercritical flow, and mixing is still possible for a Froude number less than 1. As we have shown here, a Froude number as low as 0.55 can be an appropriate threshold for instability in that most of the region of turbulent dissipation in the numerical model is captured in the ray tracing algorithm. It has been noted in the literature that mixing is possible for Froude number smaller than unity or conversely, for Richardson number larger than 0.25 (Galperin et al., 2007). Thus, our threshold of unity may be too stringent for instability to occur. Perhaps a more moderate value of $Fr = 0.75$, safely in the range presented in Fig. 14, may be a more appropriate threshold for instability. This corresponds to a Richardson number of approximately 0.44 which is within the bounds of where instability has been observed to occur (Galperin et al., 2007).

5. Discussion

Observational studies over the past two decades have shown that canyons are efficient dissipators of internal tides (Bosley et al., 2004; Bruno et al., 2006; Gardner, 1989; Gordon and Marshall, 1976; Gregg et al., 2011; Hall and Carter, 2011; Hotchkiss and Wunsch, 1982; Lee et al., 2009a, b; Vlasenko et al., 2016; Waterhouse et al., 2013; Xu and Noble, 2009). We have conducted an idealized parameter space sweep to understand the processes leading to this energy loss and quantify this energy loss relative to the energy lost over a comparable planar section of continental slope. For the case of the flat bottom canyon, both an increase in ray and energy density via topographic focusing, as well as a nonlinear arrested lee wave over the V-shaped canyon lip, are responsible for enhanced energy loss. In the near-critical slope canyon, an increase in ray density can similarly lead to increased energy dissipation, as can an increase in vertical wavenumber. We find that for a continental slope consisting of vertical walls, the insertion of a flat bottom canyon always increases the energy lost from incoming internal tides, whereas near-critical slope canyons largely decrease the energy loss at the slope relative to a planar near-critical slope. We confirm the observational studies that canyons can be potential sinks of internal wave energy. To conduct the study we have used a ray tracing algorithm and numerical model in tandem, with the numerical model illustrating the robustness of the linear theory in understanding the fundamentals of internal wave scattering in canyons.

We have shown that energy flux divergence, dissipation, the Froude number and Richardson number can be used to quantify the effects of canyons; however there are differences between these different diagnostic quantities. In Figs. 6 and 12, the two di-

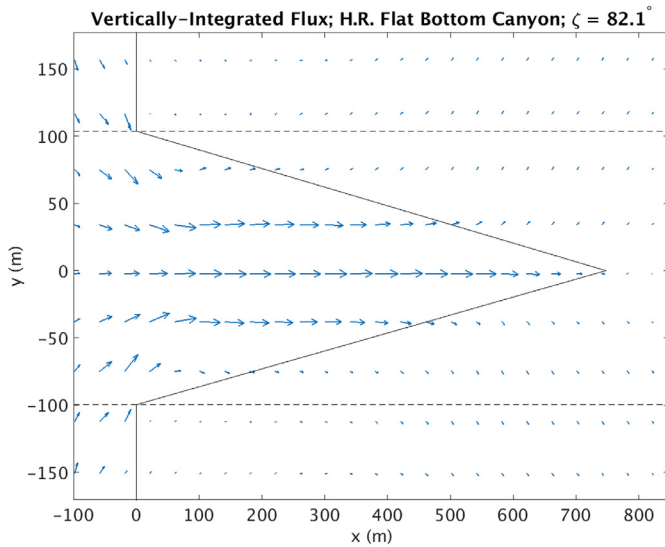


Fig. 15. Vertically integrated energy flux for the case of a flat bottom canyon with $\zeta = 82.1^\circ$ (high resolution, non-hydrostatic resolution). The energy flux calculated over the entire nine tidal cycles (i.e. after steady state reached) and tidally-averaged, as done for all divergence of the energy flux and dissipation calculations. The vectors have all been normalized by the maximum value so as to show the relative energy flux throughout the canyon domain. Dashed lines indicate the y -boundaries for the canyon energy flux divergence and dissipation calculations. (For interpretation of the references to color in this figure legend, the reader is referred to the web version of this article.)

agnostics of the divergence of the energy flux and explicit energy dissipation, \bar{E}_1 and \bar{E}_2 , respectively, are in broad agreement on the overall behavior of energy loss within the canyon regions as ζ increases. It is clear however, in Fig. 6 that \bar{E}_1 is consistently larger than \bar{E}_2 . This difference in metrics is due to the fact that we do not diagnose the numerical dissipation and energy input to mixing, which can add to this difference in diagnostics (i.e. the residual term in our energy budget, (7)). The difference in diagnostics is also most pronounced for large values of ζ where we expect that nonlinear processes, encapsulated in the residual term, will be more prevalent.

Additionally, Fig. 6 suggests that some flat bottom canyons at high ζ can dissipate more internal wave energy than impinges on the canyon region from the west. The cause of this behavior is revealed by examination of the energy flux (presented in Fig. 15): the flux into the canyon through the y -boundaries for large ζ is positive, due to the scattering and refractive effects of the canyon. Specifically waves are refracted around the canyon mouth and enter the canyon through the side boundaries, giving rise to this large inward flux. In the control simulation with flat bathymetry, there is no net flux in the y -direction.

The classes of canyons studied here are very idealized and were constructed to span the parameter space, yet provide insight relevant to real ocean canyons. In addition to obtaining a first order understanding of processes contributing to internal wave breaking in submarine canyons, many canyons, irrespective of location, are short and steep, similar to some hybrid of our two classes (Harris and Whiteway, 2011). Additionally, numerous studies have shown that regions of the continental slope are near-critical to supercritical, most noticeably the recent TTIDE study, in which most of the incoming internal tides were reflected back toward the open ocean (Johnston, Rudnick and Kelly, 2015). Thus, our construction of the relative energy loss due to canyons, relative to some continental slope, is relevant. The true energy loss enhancement by continental slope canyons may lie somewhere between that of the flat bottom and near-critical slope canyons in Fig. 12 given that the average maximum continental slope across most of the continental slope is

between critical and pure vertical (and may be two to eight times that lost on a planar supercritical continental slope).

Another idealization is the generation of the internal wave normal to the topography. While this is a departure from reality, it allows us to obtain symmetric dissipation on both sides of the canyon and gain intuition into the focusing efficiency of the canyons as a function of the canyon aspect ratio. This simplification does not, however, alter the underlying physics of the problem. As this scenario is not our focus here, we leave this as another potential application of the ray tracing algorithm.

In addition to the chosen canyon topography, further simplifications were made in ignoring the effects of rotation. A main consideration in ignoring the effects of rotation is the Rossby number, or the ratio of the advective to rotational terms in the momentum equation (formulated in Part 1), calculated as

$$Ro = \frac{U}{fL} \quad (11)$$

where U is a velocity scale, f is the Coriolis parameter and L is a length scale. When $Ro < 1$, the effects of rotation should be considered while rotation can be ignored for cases when $Ro > 1$. For our case, the forcing velocity, U , is 2 cm/s, the basin length scale, L , is approximately 1 km and a low-latitude Coriolis frequency, f , is of order 10^{-5} . This yields a Rossby number of 2, so rotation is not important. Additionally, the omission of rotation made it easier to identify a relationship between the spatial structure of energy loss, as it has been shown that rotation may lead to asymmetries in the location of dissipation within canyons (Zhang et al., 2014). Other work has shown that rotation may be an important contributor to canyon upwelling dynamics (Waterhouse et al., 2009) and resonant amplification (Swart et al., 2011), although these studies were conducted for canyon lengths much larger than those presented here, and hence by (11), of small Rossby number and thus more affected by rotation.

Additionally, we made the assumption of constant stratification in our ray tracing and numerical model setup. Our goal here, however, is not to simulate a real canyon in every aspect but to get a broader understanding of the processes occurring in canyons. Specifically, the constant stratification assumption translates to a constant angle of inclination for the group velocity vectors in the ray tracing algorithm. This simplification made the output of the ray tracing scheme significantly easier to understand and use as a tool for interpreting the MITgcm results to probe the underlying physics.

6. Conclusion

There have been extensive numerical modeling studies regarding internal tide energy loss at a variety of topographic features, yet submarine canyons, specifically canyons on the continental slope, have not received sufficient attention. As a first attempt to study the underlying physical processes and understand the topographic control on the ability of these canyons to induce mixing, we have conducted a parameter space study for idealized V-shaped canyons. The two topographic parameters that we have investigated are the thalweg steepness, related to angle α_t , which included two cases: near-critical and pure vertical walls, as well as the ratio of canyon width to canyon length, related to angle ζ , which we allowed to vary between 0° and 90° . Both energy loss diagnostics, the divergence of the energy flux and the dissipation, yield the same behavior for the parameter space; that is, as ζ increases, the percentage of incoming energy that is lost due to the canyon remains approximately constant and then, around $\zeta = 30^\circ$, for vertical side walls, begins to increase and peaks just before $\zeta = 83^\circ$, at which point it decreases. This behavior in ζ has some α -dependence as the near-critical slope canyons exhibits a small dip in energy loss centered around the same transition point

of $\zeta = 83^\circ$ before increases slightly for the narrowest canyons. Parameter α is also of equal importance to ζ when comparing the energy lost in the canyon to some plane continental slope.

To explain these three distinct regimes and their associated physics, we use our ray tracing algorithm (described in Part 1), as well as calculate the Richardson number from the MITgcm simulations. For the first regime ($\zeta < 30^\circ$ for flat bottom canyons and $\zeta < 45.8^\circ$ for near-critical slope canyons), energy loss remained roughly constant with ζ as less wave energy is able to propagate into the canyon region as it becomes narrower. Energy loss increases steeply with ζ in the second regime, as secondary wave reflections within the canyon are possible. For the near-critical slope canyon case, this means that there are more opportunities to increase the vertical wavenumber, thereby leading to instability. The near-critical slope canyon has a small dip in energy loss in Regime 2 around $\zeta = 80^\circ$ as the ray density increase becomes less of a factor in energy loss and the relative importance of increases in vertical wave number rises. Both the flat bottom and near-critical slope cases also achieve an increase in Froude number in this regime through an increase in wave density within the canyon region. The significant increase in energy loss with ζ that characterizes Regime Two is sharply halted for the flat bottom canyons around $\zeta = 83^\circ$, at which point energy loss falls off as ζ approaches 90° . For the near-critical slope canyons, there is still a slight uptick in energy loss as ζ approaches 90° owing to further increase in vertical wave number. In this third regime, although the wave can undergo many reflections, the canyon has become so narrow that relatively little wave energy can make it into the canyon region. It should also be noted that, for all regimes, the flat bottom canyons achieve energy loss due to a breaking lee wave mechanism at the steep wall edge enhanced by the increased ray density (Klymak et al., 2013). Thus, the three primary mechanisms for instability and mixing (increased ray and thus energy density, increased vertical wave number and the presence of lee waves) all combine in different regimes to lead to significant energy loss. Such canyons can dissipate up to nearly 100% of the incoming internal tide energy and can be more efficient pathways for dissipation, especially in the second ζ regime, than the surrounding continental slope.

In comparing the spatial extent of instability, and thus potential extent for mixing, we have shown that the agreement between the extent of wave-breaking in the linear ray tracing algorithm (diagnosed from the Froude number) and the numerical model (diagnosed from both the Richardson number and turbulent dissipation) is variable based on the canyon geometry and the threshold for instability. The ray tracing can indicate where energy density increases, and how the vertical wavenumber changes. The full numerical simulations, however, include nonlinear processes, such as wave breaking, dissipation and mixing, as well as allowing for constructive and destructive interference. Hence the ray tracing can provide qualitative guidance as to the dependence of focusing on the canyon aspect ratio (see Fig. 7) and aid in the interpretation of the numerical simulations, but the numerical simulations are necessary to quantitatively determine the dissipation and its spatial distribution. This is the first time that ray tracing has been used to calculate quantities such as the vertical wavenumber, ray density and, subsequently, the Froude number. Given that there is a reasonable qualitative agreement with the models, the ray tracing may be used as a precursor to a GCM or observational campaign, to identify whether instabilities occur for given topography and where those instabilities occur. The ray tracing algorithm does not require significant computational power or time and may thus be a powerful tool in considering whether GCM-scale simulations or field programs should be conducted, as well as the scope of such simulations or observations.

Although this is an idealized study, it is an important first step toward characterizing the dissipative effects of continental slope

canyons. The validity of these results can be tested in realistic continental slope canyons. If validated, this additional mixing could have important implications for ocean stratification and circulation. The spatial distribution of diapycnal mixing may be altered when the elevated levels of dissipation within continental slope canyons are accounted for and may only be accurately captured when we include all potential sinks of internal tidal energy in GCMs (Melet et al., 2016).

Acknowledgments

The authors thank Stephen Griffies and Robert Hallberg for reviewing early versions of this manuscript, two anonymous reviewers for their helpful comments as well as Angelique Melet and Ben Mater for insightful conversations. This report was prepared by Robert Nazarian under award NA08OAR4320752 from the National Oceanic and Atmospheric Administration, U.S. Department of Commerce. The statements, findings, conclusions, and recommendations are those of the authors and do not necessarily reflect the views of the National Oceanic and Atmospheric Administration or the U.S. Department of Commerce.

References

- Bosley, K., Lavelle, J., Brodeur, R., Wakefield, W., Emmett, R., Baker, E., Rehmke, K., 2004. Biological and physical processes in and around astoria submarine canyon, Oregon, USA. *J. Marine Syst.* 50, 21–37.
- Bruno, M., Vazquez, A., Gomez-Enri, J., Vargas, J., Lafuente, J., Ruiz-Canavante, A., Mariscal, L., Vidal, J., 2006. Observations of internal waves and associated mixing phenomena in the portimao canyon area. *Deep Sea Res.* 53, 1219–1240.
- Buijsman, M., Legg, S., Klymak, J., 2012. Double-ridge internal tide interference and its effect on dissipation in Luzon strait. *J. Phys. Oceanogr.* 42, 1337–1356.
- Codiga, D., Renouard, D., Fincham, A., 1999. Experiments on waves trapped over the continental slope and shelf in a continuously stratified rotating ocean. *J. Marine Res.* 57, 585–612.
- Cummins, P., Oey, L., 1997. Simulation of barotropic and baroclinic tides off northern british columbia. *J. Phys. Oceanogr.* 27, 762–781.
- Galperin, B., Sukoriansky, S., Anderson, P., 2007. On the critical richardson number in stably stratified turbulence. *Atmos. Sci. Lett.* 8, 65–69.
- Gardner, W., 1989. Periodic resuspension in baltimore canyon by focusing of internal waves. *J. Geophys. Res.* 94, 18185–18194.
- Gordon, R., Marshall, N., 1976. Submarine canyons: internal wave traps? *Geophys. Res. Lett.* 3, 622–624.
- Gregg, M.C., Hall, R.A., Carter, G.S., Alford, M.H., Lien, R.-C., Winkel, D.P., Wain, D.J., 2011. Flow and mixing in Ascension, a steep, narrow canyon. *J. Geophys. Res.* 116 (C07016). doi:10.1029/2010JC006610.
- Hall, R., Carter, G., 2011. Internal tides in monterey submarine canyon. *J. Phys. Oceanogr.* 41, 186–204.
- Harris, P., Whiteway, R., 2011. Global distribution of large submarine canyons: geomorphic differences between active and passive continental margins. *Marine Geo.* 285, 69–86.
- Hotchkiss, F., Wunsch, C., 1982. Internal waves in hudson canyon with possible geological implications. *Deep Sea Res.* 29, 415–442.
- Ivey, G., Nokes, R., 1989. Vertical mixing due to the breaking of critical internal waves on sloping boundaries. *J. Fluid Mech.* 204, 479–500.
- Johnston, T., Rudnick, D., Kelly, S., 2015. Standing internal tides in the Tasman sea observed by gliders. *J. Phys. Oceanogr.* 45, 2715–2737.
- Kang, D., Fringer, O., 2012. Energetics of barotropic and baroclinic tides in the monterey bay area. *J. Phys. Oceanogr.* 42, 272–290.
- Klymak, J., Buijsman, M., Legg, S., Pinkel, R., 2013. Parameterizing baroclinic internal tide scattering and breaking on supercritical topography: the one- and two-ridge cases. *J. Phys. Oceanogr.* 43, 1380–1397.
- Kurapov, A., Egbert, G., Allen, J., Miller, R., Erofeeva, S., Kosro, P., 2003. The m2 internal tide off oregon: inferences from data assimilation. *J. Phys. Oceanogr.* 33, 1733–1757.
- Lamb, K., Farmer, D., 2011. Instabilities in an internal solitary-like wave on the oregon shelf. *J. Phys. Oceanogr.* 41, 67–87.
- Lee, I.-H., Lien, R.-C., Liu, J., Chuang, W.-S., 2009a. Turbulent mixing and internal tides in Gaoping (Kaoping) submarine canyon, taiwan. *J. Marine Syst.* 76, 383–396.
- Lee, I.-H., Wang, Y.-H., Liu, J., Chuang, W.-S., Xu, J., 2009b. Internal tidal currents in the Gaoping (Kaoping) submarine canyon. *J. Marine Syst.* 76, 397–404.
- Legg, S., 2014. Scattering of low-mode internal waves at finite isolated topography. *J. Phys. Oceanogr.* 44, 359–383.
- Legg, S., Adcroft, A., 2003. Internal wave breaking at concave and convex continental slopes. *J. Phys. Oceanogr.* 33, 2224–2246.
- Maas, L., Benielli, D., Sommeria, J., Lam, F., 1997. Observation of an internal wave attractor in a confined, stably stratified fluid. *Nature* 388, 557–561.

- MacKinnon, J., Alford, M., Sun, O., Pinkel, R., Zhao, Z., Klymak, J., 2013. Parametric subharmonic instability of the internal tide at 29 degrees n. *J. Phys. Oceanogr.* 43, 17–28.
- Marshall, J., Adcroft, A., Hill, C., Perelman, L., Heisey, C., 1997. A finite-volume, incompressible Navier–Stokes model for studies of the ocean on parallel computers. *J. Geophys. Res.* 102, 5753–5766.
- Melet, A., Legg, S., Hallberg, R., 2016. Climatic impacts of parameterized local and remote tidal mixing. *J. Clim.* 29, 3473–3500.
- Nazarian, R.H., Legg, S., 2017a. Internal wave scattering in continental slope canyons, part 1: Theory and development of a ray tracing algorithm. *Ocean Modeling* 118 in press.
- Nikurashin, M., Legg, S., 2011. A mechanism for local dissipation of internal tides generated at rough topography. *J. Phys. Oceanogr.* 41, 378–395.
- Petruncio, E., Rosenfeld, L., Paduan, J., 1998. Observations of the internal tide in monterey canyon. *J. Phys. Oceanogr.* 28, 1873–1903.
- Polzin, K., 2008. Mesoscale eddy-internal wave coupling. part i: symmetry, wave capture, and results from the mid-ocean dynamics experiment. *J. Phys. Oceanogr.* 38, 2556–2574.
- Polzin, K., Toole, J., Ledwell, J., Schmitt, R., 1997. Spatial variability of turbulent mixing in the abyssal ocean. *Science* 276, 93–96.
- Swart, N., Allen, S., Greenan, B., 2011. Resonant amplification of subinertial tides in a submarine canyon. *J. Geophys. Res. Oceans* 116.
- Vlasenko, V., Stashchuk, N., Inall, M., Porter, M., Aleynik, D., 2016. Focusing of baroclinic tidal energy in a canyon. *J. Geophys. Res.* 121, 2824–2840.
- Waterhouse, A.F., Allen, S.E., Bowie, A.W., 2009. Upwelling flow dynamics in long canyons at low Rossby number. *J. Geophys. Res.* 114 (C05004). doi:10.1029/2008JC004956.
- Waterhouse, A., Tutak, B., Valle-Levinson, A., Sheng, Y.-P., 2013. Influence of two tropical storms on the residual flow in a subtropical tidal inlet. *Estuaries Coasts* 36, 1037–1053.
- Xu, J.P., Noble, M.A., 2009. Currents in Monterey Submarine Canyon. *J. Geophys. Res.* 114 (C03004). doi:10.1029/2008JC004992.
- Yih, C., 1980. Stability of stratified flows. 1: General results. 2: Instability as a result of resonance. 3: Stability of stationary internal waves. Thermo-Hydrodynamic Instability: Theory and Applications. Von Karman Institute for Fluid Dynamics.
- Zhang, W., Duda, T., Udovychenkov, I., 2014. Modeling and analysis of internal-tide generation and beam-like onshore propagation in the vicinity of shelfbreak canyons. *J. Phys. Oceanogr.* 44, 834–849.